The Astrophysical Journal, 723:1748–1761, 2010 November 10 doi:10.1088/0004-637X/723/2/1748


# THE SOFT X-RAY AND NARROW-LINE EMISSION OF Mrk 573 ON KILOPARSEC SCALES

O. Gonzalez-Martin[1,2], J. A. Acosta-Pulido[3,4], A. M. Perez Garcia[3,4], and C. Ramos Almeida[5]
[1] IESL, Foundation for Research and Technology, 71110 Heraklion, Crete, Greece; omaira@physics.uoc.gr
[2] Department of Physics, University of Crete, Voutes, 71003 Heraklion, Crete, Greece
[3] Instituto de Astrofísica de Canarias (IAC), C/Vía Láctea, s/n E-38205, La Laguna, Tenerife, Spain; jap@iac.es, apg@iac.es
[4] Departamento de Astrofísica, Universidad de La Laguna, E-38205 La Laguna, Tenerife, Spain
[5] Department of Physics & Astronomy, University of Sheffield, Sheffield, S3 7RH, UK; C.Ramos@sheffield.ac.uk
*Received 2010 January 22; accepted 2010 September 12; published 2010 October 26*

## ABSTRACT

We present a study of the circumnuclear region of the nearby Seyfert galaxy Mrk 573 using *Chandra*, *XMM-Newton*, and *Hubble Space Telescope* (*HST*) data. We have studied the morphology of the soft (<2 keV) X-rays comparing it with the [O III] and H$\alpha$ *HST* images. The soft X-ray emission is resolved into a complex extended region. The X-ray morphology shows a biconical region extending up to 12 arcsec (4 kpc) in projection from the nucleus. A strong correlation between the X-rays and the highly ionized gas seen in the [O III]$\lambda$5007 Å image is reported. Moreover, we have studied the line intensities detected with the *XMM-Newton* Reflection Grating Spectrometer (RGS) and used them to fit the low-resolution EPIC/*XMM-Newton* and ACIS/*Chandra* spectra. The RGS/*XMM-Newton* spectrum is dominated by emission lines of C VI, O VII, O VIII, Fe XVII, and Ne IX, among other highly ionized species. A good fit is obtained using these emission lines found in the RGS/*XMM-Newton* spectrum as a template for *Chandra* spectra of the nucleus and extended emission, coincident with the cone-like structures seen in the [O III]/H$\alpha$ map. The photoionization model Cloudy provides a reasonable fit for both the nuclear region and the cone-like structures showing that the dominant excitation mechanism is photoionization. For the nucleus the emission is modeled using two phases: a high ionization [log ($U$) = 1.23] and a low ionization [log ($U$) = 0.13]. For the high-ionization phase the transmitted and reflected components are in a 1:2 ratio, whereas for the low ionization the reflected component dominates. For the extended emission, we successfully reproduced the emission with two phases. The first phase shows a higher ionization parameter for the northwest (log ($U$) = 0.9) than for the southeast cone (log ($U$) = 0.3). Moreover, this phase is transmission dominated for the southeast cone and reflection dominated for the northwest cone. The second phase shows a low-ionization parameter (log ($U$) = −3) and is rather uniform for northwest and southeast cones and equally distributed in reflection and transmission components. In addition, we have also derived the optical/infrared spectral energy distribution (SED) of the nucleus from high spatial resolution images of Mrk 573. The nuclear optical/infrared SED of the nucleus has been modeled by a clumpy torus model. The torus bolometric luminosity agrees very well with the active galactic nucleus (AGN) luminosity inferred from the observed hard X-ray spectrum. The optical depth along the line of sight expected from the torus modeling indicates a high neutral hydrogen column density in agreement with the classification of the nucleus of Mrk 573 as a Compton-thick AGN.

*Key words:* galaxies: active – galaxies: individual (Mrk 573) – galaxies: nuclei – galaxies: Seyfert – infrared: galaxies

*Online-only material:* color figures

## 1. INTRODUCTION

Visible signatures of the direct interaction between the active galactic nuclei (AGNs) and their host galaxies include kpc-scale [O III]- and H$\alpha$-emitting regions, the so-called extended narrow-line region (ENLR), which is observed in many nearby Seyfert galaxies (Schmitt et al. 2003; Veilleux et al. 2003; Whittle & Wilson 2004; Ramos Almeida et al. 2006). Understanding the AGN-host galaxy interaction and feedback is crucial for the study of both galaxy and AGN evolution (Silk & Rees 1998; Kauffmann et al. 2003; Hopkins et al. 2006; Schawinski et al. 2007, 2009).

One of the most promising ways to study these interactions is through soft X-rays (Crenshaw et al. 1999, 2003; Dai et al. 2008). In the unified picture of AGNs (Antonucci 1993) the soft X-ray spectra of type 2 Seyfert galaxies are expected to be affected by emission and scattering from the medium, which is also strongly influenced by the nuclear continuum. However, soft X-rays can also be produced through mechanical heating, as in shocks driven by supernova explosions in nuclear star-forming regions. Indeed, it is quite plausible that both effects are important (e.g., Mrk 3; Sako et al. 2000). This soft X-ray emission provides the opportunity to obtain an X-ray diagnostic for the physical properties of the interacting interstellar medium (ISM; Young et al. 2001; Yang et al. 2001; Ogle et al. 2000, 2003; Bianchi et al. 2006; Evans et al. 2006; Kraemer et al. 2008).

The galaxy Mrk 573 has been extensively studied by many authors. Its active nucleus is hosted in an (R)SAB(rs)0+ galaxy.[6] Mrk 573 is well known for its extended, richly structured circumnuclear emission-line regions (Tsvetanov & Walsh 1992). It has long been known to show a biconical structure, bright arcs, and knots of line-emitting gas (Ferruit et al. 1999; Quillen et al. 1999) that are strongly aligned and interacting with a kiloparsec-scale low-power radio outflow (Pogge & De Robertis 1993; Falcke et al. 1998; Ferruit et al. 1999). Schlesinger et al. (2009) have recently studied the STIS/*Hubble Space Telescope* (*HST*) spectrum, finding that the ENLR optical spectrum is consistent with photoionization by the AGN.

[6] The redshift of the galaxy has been measured to be $z = 0.017$ (Ruiz et al. 2005), which implies a physical scale of 333 pc arcsec$^{-1}$, using $H_0 = 75$ km s$^{-1}$ Mpc$^{-1}$.

In their study of the ACIS/*Chandra* spectrum of Mrk 573, Guainazzi et al. (2005) showed that it is consistent with a Compton-thick source (i.e., $N_H > 1.6 \times 10^{-24}$ cm$^{-2}$), showing a large equivalent width of the FeK$\alpha$ emission line and a steep photon spectral index ($\Gamma = 2.7 \pm 0.4$). These characteristic X-ray properties, together with high-quality LIRIS near-infrared spectroscopy, allowed this galaxy to be reclassified as an obscured narrow-line Seyfert 1 (Ramos Almeida et al. 2008, 2009b).

Reflection Grating Spectrometer (RGS)/*XMM-Newton* high-resolution observations of Mrk 573 were reported among a sample of 69 objects by Guainazzi et al. (2008), whose spectrum shows strong emission coming from the O VII triplet and Ly$\alpha$ O VIII features (see their Figure 1), but only few emission-line fluxes were reported in their work. However, the analysis of the extended soft X-ray emission had not been previously reported in the literature.

In this paper, we discuss the extended kpc-scale emission of Mrk 573 using ACIS/*Chandra* high-resolution images, RGS/*XMM-Newton* high-resolution spectra, and *HST* imaging. While RGS/*XMM-Newton* data give the opportunity to use emission-line diagnostics to understand the nature of this emission, *Chandra* high-resolution images give the opportunity to spatially resolve the emission and study their properties separately. *HST* images allow us to establish the connection between the optical structure and the soft X-ray emission. The paper is presented as follows. Section 2 describes the data reduction and processing. We present the study of the circumnuclear morphology and the X-ray spectral analysis in Sections 3 and 4, respectively. The origin of this soft X-ray emission is discussed in Section 5 and the optical/infrared spectral energy distribution (SED) is studied in Section 6. Finally, conclusions and the overall picture for Mrk 573 are presented in Section 7.

## 2. OBSERVATIONS AND DATA PROCESSING

### 2.1. XMM-Newton Data

We retrieved from the HEASARC archive the *XMM-Newton* observation of Mrk 573 taken on 2004 January 15 (Obs. ID 0200430701). RGS data were processed with the standard RGS pipeline processing chains incorporated in the *XMM-Newton* SAS v.8.0.1 (Gabriel et al. 2004). Dispersed source and background spectra (using blank field event lists) were extracted with automatic RGS extraction tasks. The net exposure time is 9 ks after flare removal and the net count rate is 0.21 counts s$^{-1}$.

In this paper, we also used lower resolution spectrum from the EPIC pn camera (Strüder et al. 2001). Source regions were extracted within a circular region of 25 arcsec[7] radius centered at the position given by NASA/IPAC Extragalactic Database (NED).[8] We also used the EREGIONANALISE SAS task to compute the best centroid for our source. The difference between the best-fit centroid and the NED position is 2 arcsec (P.A. 126°). It implies ∼1% of error on the final flux, according to the point-spread function (PSF) of EPIC pn instrument. Background was selected from a circular region in the same chip as for the source region, excluding point sources. Regions were extracted by using the EVSELECT task and pn redistribution matrix, and effective areas were calculated with the RMFGEN and ARFGEN tasks, respectively. We also binned the EPIC/pn spectrum to give a minimum of 20 counts bin$^{-1}$ before background subtraction to be able to use the $\chi^2$ as the fit statistics using the GRPPHA task. Note that the background is only 2.4% of the total number of counts (∼ 50 counts). Thus, the spectral binning can be done before background subtraction in this source.

### 2.2. Chandra Data

Mrk 573 was observed by *Chandra* on 2006 November 11. Level 2 event data from the ACIS instrument were extracted from the *Chandra* archive[9] (Obs. ID 7745). The data were reduced with the CIAO 3.4[10] data analysis system and the *Chandra* Calibration Database (caldb 3.4.0[11]). The exposure time was processed to exclude background flares using the LC_CLEAN.SL task[12] in source-free sky regions of the same observation. The net exposure time after flare removal is 35 ks and the net count rate is 1.5 s$^{-1}$. The nucleus has not significantly piled up.

*Chandra* data include information about the photon energies and positions that was used to obtain energy-filtered images and to carry out sub-pixel resolution spatial analysis. Although the default pixel size of the *Chandra*/ACIS detector is 0.492 arcsec, smaller spatial scales are accessible as the image moves across the detector pixels during the telescope dither, therefore sampling pixel scales smaller than the default pixel of *Chandra*/ACIS detector. This allows sub-pixel binning of the images. Similar techniques were applied for the analysis of *Chandra* observations of, for example, the SN1987A remnant (Burrows et al. 2000).

In addition to the high spatial resolution analysis, we applied smoothing techniques to detect the low-contrast diffuse emission. We applied the adaptive smoothing CIAO tool CSMOOTH, based on the algorithm developed by Ebeling et al. (2006). CSMOOTH is an adaptive smoothing tool for images containing multi-scale complex structures and preserves the spatial signatures and the associated counts, as well as significance estimates. A minimum and maximum significance S/N level of 3 and 4, and a scale maximum of 2 pixels were used.

We also performed spectral analysis of the nuclear and extended emission using CIAO software. Background regions were defined by source-free apertures around the soft X-ray emission regions. Response and ancillary response files were created using the CIAO MKACISRMF and MKWARF tools. To be able to use the $\chi^2$ as the fit statistics, the spectra were binned to give a minimum of 20 counts bin$^{-1}$ before background subtraction using the GRPPHA task, included in FTOOLS.[13]

### 2.3. Optical and Near-IR Data

In order to perform a detailed comparison between X-ray and optical cone-like structures we have retrieved *HST*/WFPC2 narrowband optical images, centered at 5343 Å ([O III]) and 6510 Å(H$\alpha$). These images were obtained within the Cycle 4 program 6332 (PI: Wilson) and retrieved from the Hubble Legacy Archive. Details of the observations can be found in Falcke et al. (1998). The two images were re-centered assuming that the peak in both images corresponds to the same locus (Ferruit et al. 1999). The same assumption was used to align

[7] This radius contains the 80% (85%) of the PSF at 1.5 keV (9.0 keV) for an on-axis source with EPIC pn instrument.
[8] http://nedwww.ipac.caltech.edu/
[9] http://cda.harvard.edu/chaser/
[10] http://asc.harvard.edu/ciao
[11] http://cxc.harvard.edu/caldb/
[12] http://cxc.harvard.edu/ciao/download/scripts/
[13] http://heasarc.gsfc.nasa.gov/docs/software/ftools

**Table 1**
High Spatial Resolution Nuclear Fluxes

| $\lambda_{ref}$ ($\mu$m) | $F_\nu$ (mJy) | Instrument/Filter | Ref. |
|---|---|---|---|
| 0.675 | 0.002 | WFPC2/F675W | a |
| 0.814 | 0.003 | WFPC2/F814W | a |
| 1.100 | 0.036 | NICMOS/F110W | a |
| 1.650 | 0.479 | NICMOS/F160W | a |
| 2.120 | 3.20 | NSFCam/K′ | b |
| 3.510 | 18.8 | NSFCam/L | b |
| 4.800 | 41.3 | NSFCam/M | b |
| 10.36 | 177 | T-ReCS/N | c |
| 18.30 | 415 | T-ReCS/Qa | c |

**Notes.** Errors in flux densities are ∼10% for *HST* fluxes, ∼20% for the 3 m NASA IRTF, ∼15% for T-ReCS/N, and ∼25% for T-ReCS/Qa.
**References.** (a) This work; (b) Alonso-Herrero et al. 2003; (c) Ramos Almeida et al. 2009a.

optical and X-rays images. Note that high accuracy is not needed due to the lower *Chandra* resolution.

We have also investigated the nuclear properties of Mrk 573 in the optical and near-IR ranges, based on high spatial resolution broadband images. We have found optical and near-IR broadband images taken with the WFPC2 and NICMOS cameras on board the *HST*. In particular, we used F675W and F814W WFPC2 images (program 5746; PI: Machetto), and F110W and F160W NICMOS images (program 7867; PI: Pogge). All data were retrieved from the *Hubble* Legacy Archive. Post-pipeline images have been cleaned of cosmic rays using the IRAF task *lacos_im* (van Dokkum 2001). For the analysis we have first separated the nuclear emission from the underlying host galaxy emission. We have applied the two-dimensional image decomposition *GALFIT* program (Peng et al. 2002) to fit and subtract the unresolved component (PSF). Model PSFs were created using the TinyTim software package, which includes the optics of *HST* plus the specifics of the camera and filter system (Krist 1993). The filters used here are not contaminated by line emission except for the case of F110W, which contains strong Pa$\beta$ emission. We have used the nuclear near-IR spectrum of Mrk 573 obtained with the LIRIS spectrograph (see Ramos Almeida et al. 2009b) to subtract this emission-line contribution. The Pa$\beta$ nuclear emission (including the broad and narrow components) amounts $3.17 \times 10^{-14}$ erg cm$^{-2}$ s$^{-1}$. The corrected values of the flux obtained for the nuclear component in each filter are given in Table 1.

## 3. CIRCUMNUCLEAR MORPHOLOGY

Two broadband images using *Chandra*/ACIS data[14] were created: (1) soft band at 0.2–2 keV and (2) hard band at 2–10 keV. PSF simulations were carried out using information on the spectral distribution and off-axis location of the system as inputs to ChaRT PSF simulator.[15] Hard band (>2 keV) shows a point-like morphology, consistent with the FWHM PSF simulations, while soft band (<2 keV) shows an extended morphology (see Figure 1).

The soft X-ray image shows a complex extended emission with a bipolar structure aligned along P.A. ∼ 122° (Figure 2). It extends 8.5 arcsec to the northwest and 6.5 arcsec to the southeast. As already mentioned, Mrk 573 shows a biconical

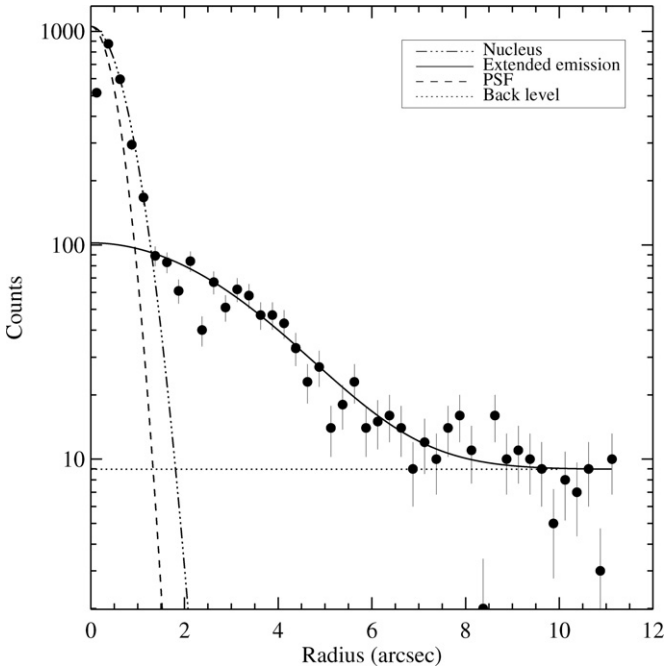


**Figure 1.** Radial profile of the soft (0.2–2.0 keV) X-ray emission of Mrk 573 (black dotted). Continuous lines correspond to the fit to the inner (< 1.5 arcsec) and outer parts of the radial profile. Dashed line shows the radial profile of the simulated PSF at ∼1 keV. The model used to fit the radial profile is of the form $y(x) = A \times e^{-x^2/2B^2}$. An additive constant was added to the outer parts of the radial profile fit to include the minimum S/N level (dotted line). The FWHM of the inner parts is 0.59 arcsec, consistent with the FWHM of the PSF (0.43 arcsec).

morphology in the [O III] emission, which resembles that observed in the soft X-rays.

The ratio of [O III] to H recombination lines is commonly assumed to be an indicator of the ionization degree in line emitting photoionized gas. We have computed the [O III]/H$\alpha$ map by dividing the flux-calibrated *HST*/WFPC2 images in those pixels where the signal-to-noise ratio (S/N) is higher than 3. A smoothing algorithm using the median within a box of 0.5 arcsec was then applied. Note that this ratio image is only used for morphological comparison and not for any quantitative analysis since the H$\alpha$ image is contaminated with [N II] emission. The use of H$\alpha$ instead of H$\beta$ to compute the ionization map could be affected by reddening variations, as shown close to the nucleus of Mrk 573. However, the extinction map (Figure 3) shows a very different morphology to that observed in the ratio [O III]/H$\alpha$ map. This implies that the basic morphology of the optical ionization map cannot be explained by differential extinction, despite a certain fraction of the emission-line map variations could be due to it.

The X-ray arc-like structure at 10 arcsec to the southeast resembles the [O III] emission. However, the X-ray emission does not show the bridge between this structure and the inner parts of the southeast cone seen in the [O III] image (also seen in [O III]/H$\alpha$). The northwest structure is coincident with the [O III] emission and strongly similar to the [O III]/H$\alpha$ morphology (see Figure 2). These facts indicate a link between the soft X-ray emission and the optical ionized gas, although the detailed structure would depend on the small-scale ionization structure of the medium.

We have also explored the circumnuclear extinction. For this purpose we have used the broadband images after subtracting the unresolved component to build a color map of the circumnuclear

[14] We used *Chandra* data for morphological analysis since it provides the best X-ray spatial resolution.
[15] http://asc.harvard.edu/chart/index.html

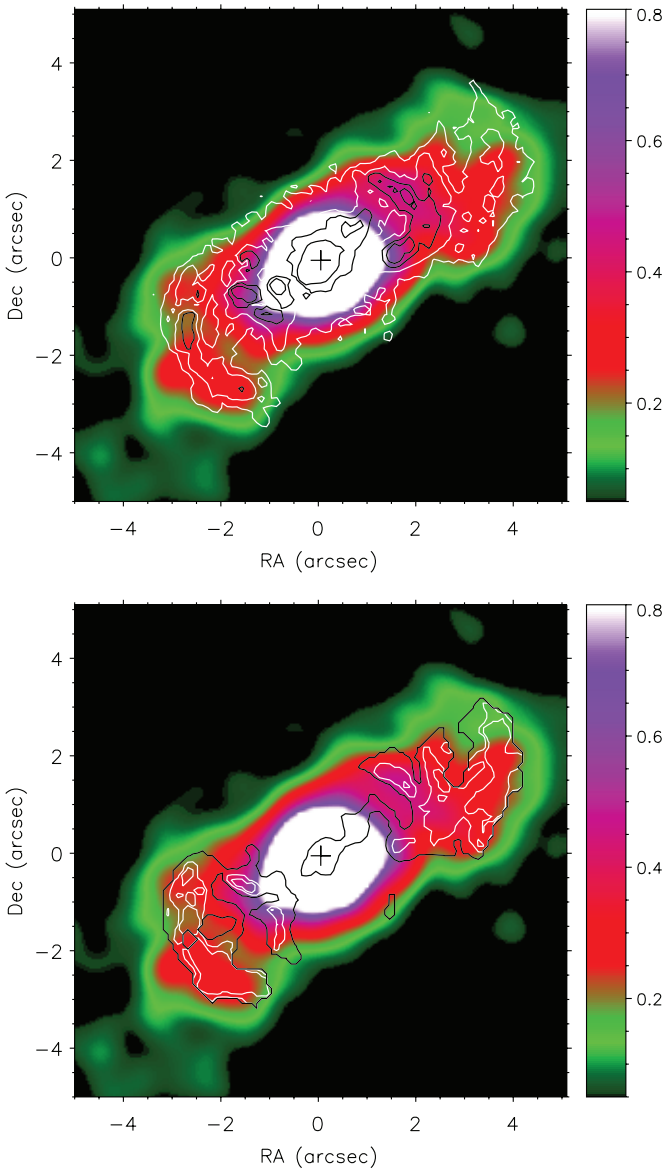


**Figure 2.** Soft 0.2–2 keV ACIS/*Chandra* image of Mrk 573. Top: [O III] contours overlaid. Bottom: [O III]/H$\alpha$ contours overlaid.

(A color version of this figure is available in the online journal.)

region of Mrk 573. The color map was created using the F814W and the F160W images, which are equivalent to the $I$ and $H$ bands, respectively. These filters were selected because they are not critically contaminated by emission lines, contrary to the color maps presented by Quillen et al. (1999). The $I-H$ map covering the central 10 arcsec is shown in Figure 3. The reddest (or darkest in black/white) regions show the location of the strongest obscuration, or equivalently, the highest dust concentration. The color map reveals a dust lane crossing the nucleus in the north–south direction, which bends after 2″ resembling incipient spiral arms. The axis delineated by this structure is oriented at about 55° with respect to the alignment of the radio structure (Falcke et al. 1998; Kinney et al. 2000, P.A. $\sim$ 125°). The radio and the dust lanes axis should be almost perpendicular if the dust lanes were the outer parts of the postulated dusty torus for type 2 nuclei. However, this is not necessarily the case, since the dust lane is observed at a much larger scale than that of the postulated torus, changes

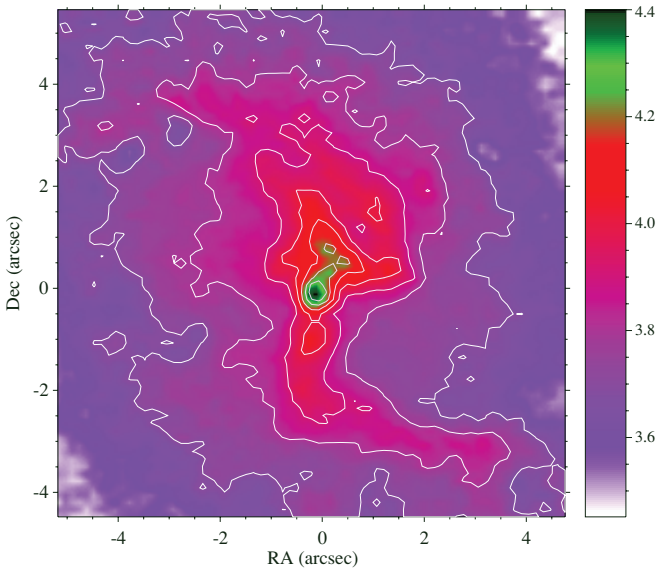


**Figure 3.** $I-H$ color map of Mrk 573. Left is the east and up is the north coordinate.

(A color version of this figure is available in the online journal.)

in the dust plane may take place when approaching the inner nucleus. On the other hand, projection effects could mask the actual orientation of both structures; for instance, Tsvetanov & Walsh (1992) proposed that the ionization cone is very inclined (35°) with respect to the plane of the sky. In addition, there is also a tongue extending 0.″5 toward the north–northwest which ends in two small blobs that resembles a structure observed in the excitation maps (see Figure 2). The presence of dust within the ionization cone has been reported before only in NGC 1068 (Bock et al. 2000). Toward the nucleus of the galaxy there is an excess of reddening which can be attributed to a natural increase in the extinction due to higher dust concentration. Assuming an intrinsic color similar to that observed in the disk of galaxies ($I-H\sim 2$; Moriondo et al. 1998), we have estimated a value of $A_V = 6.5$ mag, which results in $N_H = 1.2\times10^{22}$ cm$^{-2}$.

## 4. X-RAY SPECTRAL ANALYSIS

X-ray spectral analysis of the observed soft X-ray extended emission is crucial in determining the excitation mechanism of the plasma and its relationship to the optical bicone-like structure (see the previous section). The combination of RGS/*XMM-Newton* high spectral resolution and ACIS/*Chandra* high spatial resolution data is key to achieve this purpose. In this section, we describe in detail the methodology and main results obtained. In Section 5, we discuss the origin of this extended emission based on the results presented in this section. The analysis of the spectral counts was performed using the software package XSPEC (version 12.4.0[16]; Arnaud 1996).

### *4.1. RGS/XMM-Newton High-resolution Spectra*

Soft X-ray emission in Seyfert galaxies has been proven to consist of a plethora of emission lines plus a small fraction of continuum emission that can be described with a single flat power law (Guainazzi et al. 2008) with a fixed spectral index of $\Gamma = 1$. We obtained the emission-line fluxes of the central 30 arcsec region (note that this includes the nucleus and

[16] http://heasarc.gsfc.nasa.gov/docs/xanadu/xspec/

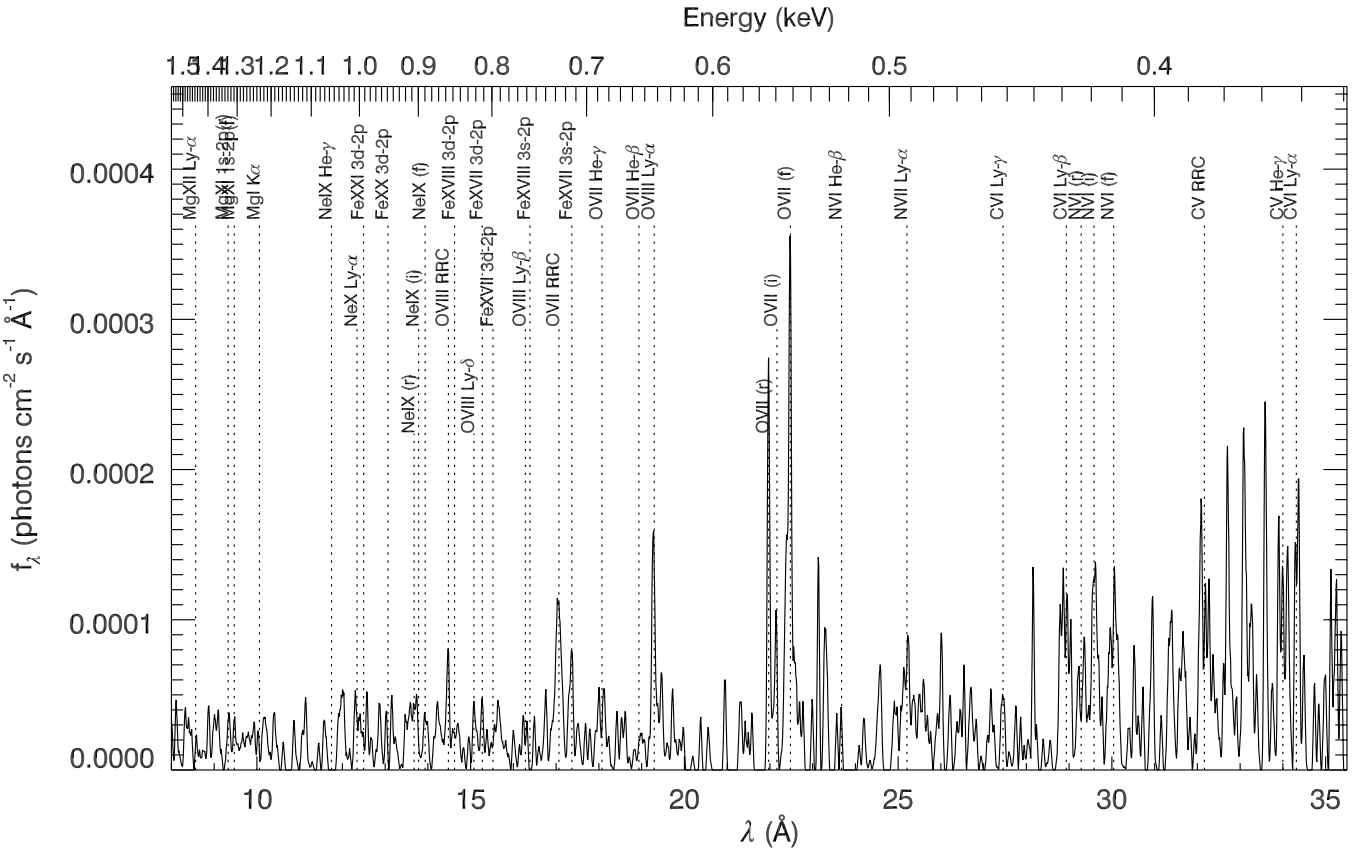


**Figure 4.** High-resolution spectrum of Mrk 573 obtained with the RGS/*XMM-Newton* instrument.

circumnuclear emission) using the RGS/*XMM-Newton* data. We searched for the presence of the 37 emission lines of C, O, N, Si, Mg, and Fe species by fitting the spectra of the two RGS cameras to Gaussian profiles together with a continuum. We used Cash statistic for this purpose.

The triplet fits were performed keeping the relative distance between centroids in energy and the centroid energy was left as a free parameter. A line was considered detected when the flux was higher than 0 at the $1\sigma$ level. The resulting RGS spectrum and detected emission lines are presented in Figure 4 and Table 2, respectively. All energy centroids are consistent with the laboratory value given the error bars. Guainazzi et al. (2008) previously studied the RGS/*XMM-Newton* spectra of Mrk 573. Unfortunately, they only reported some of the lines, all of them agreeing with our emission-line fluxes. The most intense emission lines comprising the RGS/*XMM-Newton* spectrum are C VI Ly$\beta$, O VII (r), O VII (f), O VIII Ly$\alpha$, O VII H$\gamma$, O VII RRC, Fe XVII 3*d*–2*p*, and Ne IX (r).

### 4.2. EPIC/XMM-Newton Low-resolution Spectra

The fit of EPIC/*XMM-Newton* data with a thermal model produces poor results below 2 keV ($\chi^2$ ~16). Instead, a model composed of multiple emission lines was tried. Taking advantage of the RGS/*XMM-Newton* fit, we imposed that the intensity of the lines in the low-resolution spectra fit do not exceed the RGS measurements. This is acceptable because the cross-calibrations between EPIC and RGS instruments show a normalization constant in the range of 0.9–1.0 (see Plucinsky et al. 2008). The assumed Gaussian width is 100 eV. Note that for EPIC (and also ACIS/*Chandra*) data we do not question the existence of the emission lines detected on the RGS/*XMM-Newton* but we use them as a template. Triplets were fitted using the total flux of all components of the He-like lines O VII, N VI, and Ne IX. The continuum emission was fitted to a power law to be consistent with the high spectral resolution

**Table 2**
Emission Lines Detected in the RGS/*XMM-Newton* Spectrum

| Name | $\lambda_{rest}$ (Å) | Energy (keV) | Flux ($10^{-5}$) |
|---|---|---|---|
| C V He$\gamma$ | 33.426 | 0.376 | $10.7^{27.3}_{0.00}$ |
| N VI He$\alpha$ (f) | 29.534 | 0.420 | $0.00^{82.7}_{0.00}$ |
| N VI He$\alpha$ (i) | 29.083 | 0.426 | $2.64^{57.6}_{0.00}$ |
| N VI He$\alpha$ (r) | 28.787 | 0.431 | $0.00^{1.85}_{0.00}$ |
| C VI Ly$\beta$ | 28.466 | 0.436 | $3.18^{7.10}_{0.57}$ |
| N VII Ly$\alpha$ | 24.781 | 0.500 | $1.03^{2.51}_{0.00}$ |
| O VII He$\alpha$ (f) | 22.101 | 0.561 | $5.17^{9.21}_{2.33}$ |
| O VII He$\alpha$ (i) | 21.803 | 0.569 | $0.00^{2.06}_{0.00}$ |
| O VII He$\alpha$ (r) | 21.602 | 0.574 | $3.76^{7.58}_{0.96}$ |
| O VIII Ly$\alpha$ | 18.969 | 0.654 | $2.17^{3.70}_{1.00}$ |
| O VII He$\gamma$ | 17.768 | 0.698 | $1.60^{3.36}_{0.31}$ |
| Fe XVII 3*s*–2*p* | 17.078 | 0.726 | $0.75^{1.84}_{0.00}$ |
| O VII RRC | 16.771 | 0.739 | $1.07^{2.65}_{0.03}$ |
| Fe XVII 3*d*–2*p* | 15.010 | 0.826 | $0.65^{1.45}_{0.02}$ |
| O VIII RRC | 14.228 | 0.882 | $0.48^{1.33}_{0.00}$ |
| Ne IX(f) | 13.698 | 0.905 | $0.22^{0.94}_{0.00}$ |
| Ne IX(i) | 13.552 | 0.915 | $0.12^{1.10}_{0.00}$ |
| Ne IX(r) | 13.447 | 0.922 | $0.76^{1.87}_{0.08}$ |

**Note.** [a] Units are photons cm$^{-2}$ s$^{-1}$.

**Table 3**
Measured Fluxes for EPIC/*XMM-Newton* and ACIS/*Chandra* Spectra

| Line | $\lambda_{rest}$ | Energy | *XMM-Newton* | *Chandra* | | |
|---|---|---|---|---|---|---|
| | | | | Nucleus | Cone Northwest | Cone SE |
| | (Å) | (keV) | $(10^{-5})^a$ | $(10^{-5})^a$ | $(10^{-6})^a$ | $(10^{-6})^a$ |
| Norm (pw) | | | $3.1^{3.7}_{2.4}$ | $2.5^{2.9}_{2.2}$ | ... | ... |
| C v He$\gamma$ | 33.43 | 0.371 | $18.6^{22.0}_{14.8}$ | $12.1^{16.6}_{6.9}$ | $12.6^{22.5}_{0.0}$ | $27.9^{53.8}_{2.0}$ |
| N vi triplet | 28.79/29.08/29.53 | 0.426 | $0.9^{3.6}_{0.0}$ | $2.5^{7.1}_{0.0}$ | $1.5^{13.1}_{0.0}$ | ... |
| C vi Ly$\beta$ | 28.47 | 0.436 | $7.4^{9.4}_{1.7}$ | $2.3^{5.6}_{0.0}$ | $2.6^{10.6}_{0.0}$ | ... |
| N vii Ly$\alpha$ | 24.78 | 0.500 | $7.0^{8.3}_{5.7}$ | $5.3^{6.6}_{4.4}$ | $3.7^{7.6}_{0.0}$ | $4.5^{7.9}_{1.0}$ |
| O vii triplet | 21.60/21.80/22.10 | 0.569 | $8.7^{9.9}_{7.5}$ | $7.8^{9.2}_{6.4}$ | $6.9^{10.9}_{5.0}$ | $7.7^{12.2}_{3.2}$ |
| O viii Ly$\alpha$ | 18.97 | 0.654 | $3.5^{4.7}_{2.4}$ | $2.3^{2.9}_{1.4}$ | $0.5^{2.2}_{0.0}$ | $1.5^{3.7}_{0.0}$ |
| O vii He$\gamma$ | 17.77 | 0.698 | $1.2^{2.8}_{0.2}$ | $0.0^{1.4}_{0.0}$ | $0.0^{2.20}_{0.0}$ | ... |
| Fe xvii $3s2$ | 17.08 | 0.726 | $1.2^{2.2}_{0.0}$ | $1.6^{2.2}_{0.1}$ | $2.4^{3.67}_{0.0}$ | $1.7^{4.0}_{0.0}$ |
| O vii RRC | 16.77 | 0.775 | $1.0^{1.9}_{0.1}$ | $0.8^{1.5}_{0.0}$ | $1.8^{3.64}_{0.0}$ | $1.6^{3.3}_{0.0}$ |
| Fe xvii $3d2p$ | 15.01 | 0.826 | $1.7^{2.2}_{0.7}$ | $0.0^{1.7}_{0.0}$ | $0.0^{2.89}_{0.0}$ | ... |
| O viii RRC | 14.23 | 0.871 | $[1.6^{2.0}_{1.0}]$ [b] | $1.5^{2.6}_{0.0}$ | $4.08^{5.15}_{0.43}$ | $1.0^{1.8}_{0.2}$ |
| Ne ix triplet | 13.45/13.55/13.70 | 0.905 | $2.5^{3.0}_{1.7}$ | $2.2^{2.6}_{1.6}$ | $0.0^{3.1}_{0.0}$ | ... |
| Fe xx $3d2p$ | 12.85 | 0.965 | $0.1^{0.6}_{0.0}$ | $0.32^{0.70}_{0.02}$ | $0.76^{1.65}_{0.01}$ | $0.6^{1.0}_{0.1}$ |
| Ne x Ly$\alpha$ | 12.13 | 1.022 | $1.3^{1.6}_{1.0}$ | $1.1^{1.3}_{0.9}$ | $1.3^{2.1}_{0.4}$ | |
| Ne ix He$\gamma$ | 10.97 | 1.130 | $[0.7^{0.8}_{0.4}]$ [c] | $0.44^{0.59}_{0.29}$ | $0.7^{1.3}_{0.0}$ | $0.9^{1.3}_{0.4}$ |
| Ne ix He$\delta$ | 10.69 | 1.160 | $0.8^{1.0}_{0.6}$ | ... | ... | ... |
| Ne x Ly$\beta$ | 10.16 | 1.220 | $[0.3^{0.5}_{0.1}]$ [c] | $0.33^{0.46}_{0.20}$ | $0.13^{0.6}_{0.0}$ | $0.02^{0.5}_{0.0}$ |
| Mg xi triplet | 9.17/9.31 | 1.352 | $0.4^{0.6}_{0.2}$ | $0.41^{0.52}_{0.30}$ | $0.5^{0.8}_{0.2}$ | $0.45^{0.7}_{0.2}$ |
| Si xiii triplet | 6.65/6.74 | 1.840 | $0.5^{2.8}_{0.0}$ | $0.11^{0.19}_{0.02}$ | $2.0^{3.1}_{0.9}$ | ... |

**Notes.**
[a] Units are photons $cm^{-2}$ $s^{-1}$.
[b] This value was obtained by setting the nearby line Fe xvii to zero.
[c] These values were computed after including Ne ix He$\gamma$ and Ne x Ly$\beta$, instead of Ne ix He$\delta$.

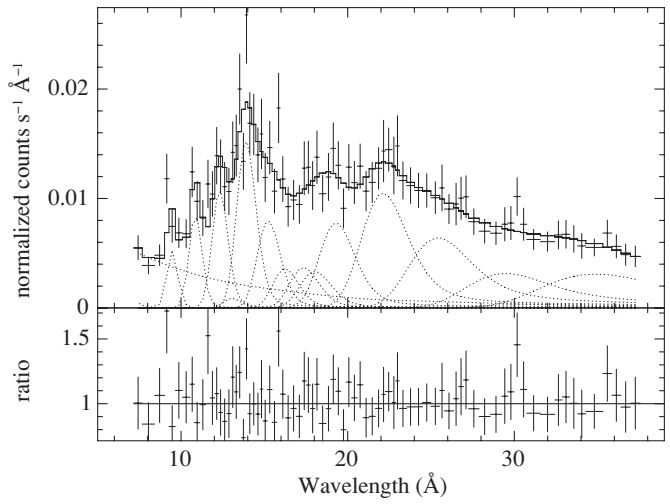


**Figure 5.** Spectral fits (top panel) and residuals (bottom panel) for the nuclear spectrum of Mrk 573 using low-resolution EPIC pn/*XMM-Newton* data. Dotted lines show the Gaussian components used to fit the spectrum.

analysis. However, this fit has poor statistics ($\chi^2_r > 2$). Five lines were added at energies above 0.95 keV in order to achieve an acceptable fit ($\chi^2_r = 0.8$): Fe xx at 0.97 keV ($\chi^2_r = 5.64$), Ne x Ly$\alpha$ at 1.02 keV ($\chi^2_r = 5.62$), Ne ix He $\delta$ at 1.16 keV ($\chi^2_r = 3.72$), Mg xi triplet at ~1.33 keV ($\chi^2_r = 0.82$), and Si xiii triplet at 1.84 keV($\chi^2_r = 0.80$). The final fit is shown in Figure 5. The low spectral resolution EPIC/*XMM-Newton* spectrum shows the following intense emission lines: C v He$\gamma$, C vi Ly$\beta$, N vii Ly$\alpha$, O vii triplet, O viii Ly$\alpha$, O vii He$\gamma$, O vii RRC, Fe xvii $3d$–$2p$, and Ne ix triplet, Ne x Ly$\alpha$, Ne ix He $\delta$, and Mg xi triplet. In the best-fit model, the flux of the O viii RRC feature appears negligible and the adjacent line Fe xvii $3d2p$ is present. This is in contrast to what happens in the ACIS/*Chandra* nuclear spectrum (see Section 4.3 and Table 3). In order to check the compatibility of the results of both spectra, we have imposed a zero intensity to the line Fe xvii $3d2p$ finding a good fit. In this case, the O viii RRC feature shows a similar flux compared to the flux reported using the *Chandra* nuclear spectrum. It is very likely that both features share the flux as measured in the RGS/*XMM-Newton* spectrum, although they cannot be distinguished in the low-resolution spectra. The best-fit model has an absorbed 0.5–2.0 keV flux of $F_{0.5-2.0\,keV} = 3.38$ (3.37–3.83) $\times 10^{-13}$ erg $s^{-1}$ $cm^{-2}$, corresponding to an unabsorbed rest frame luminosity of $L_{0.5-2.0\,keV} = 2.0$ (1.9–2.2) $\times 10^{41}$ erg $s^{-1}$. We have only included Galactic absorption in our model, which corresponds to $N_H = 2.52 \times 10^{20}$.

### *4.3. ACIS/Chandra Spectra*

We cannot separate the contribution of the northwest and southeast regions to the RGS or EPIC/*XMM-Newton* spectra. However, this is possible by using the lower spectral resolution but better spatial resolution of ACIS/*Chandra* data.

We extracted spectra from the nucleus ($R = 1$ arcsec) and two conical regions coincident with the extension of the emission, as seen in Figure 6. All extraction regions were centered at (R.A., decl.) = 01:43:57.78,+02:20:59.4. For the conical regions, we

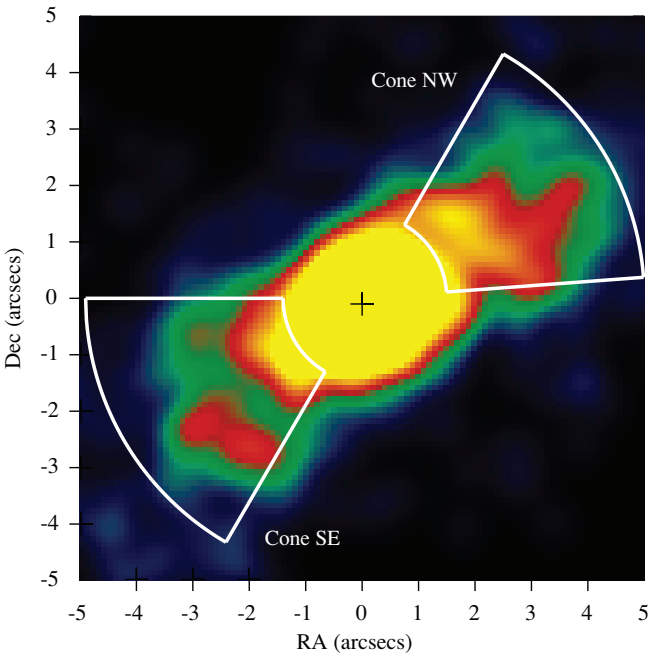


**Figure 6.** Soft (0.2–2 keV) X-ray *Chandra* image with the two extracted regions (northwwest and southeast) overplotted.

(A color version of this figure is available in the online journal.)

used an annulus, centered at the same position than the nucleus, with an inner and outer radius of 1.5 and 5 arcsec, respectively. The cones are defined by an opening angle of 60° centered at P.A. = 325° (cone northwest) and at P.A. = 145° (cone southeast).

The study of the emission above 2 keV is beyond the scope of this paper since the nucleus dominates there and it has been already well studied before (Guainazzi et al. 2005). Therefore, channels above ∼2 keV were ignored in the spectral fit. Again, the thermal model gives a poor fit with some residuals below 2 keV ($\chi^2 \sim 3$ for both cone regions).

We used the same model reported in the RGS/*XMM-Newton* spectrum assuming the emission-line fluxes found in that case, as upper limits to fit the nucleus, and the northwest and southeast cone-like structures (the same as the EPIC/*XMM-Newton* data mentioned in the previous section). Moreover, the power-law component was removed in the cone-like structures because we expect this component to be detectable only in the nuclear region. The assumed Gaussian width is 100 eV. The spectra are shown in Figure 7 and final emission-line fluxes are reported in Table 3.

Most of the emission lines in the EPIC/*XMM-Newton* spectrum are also detected in the nuclear spectrum using *Chandra* data (C V H$\gamma$, N VII Ly$\alpha$, O VII triplet, O VIII Ly$\alpha$, Ne IX triplet, Ne X Ly$\alpha$, and Mg XI triplet). Five of them were present only in the EPIC/*XMM-Newton* spectrum (C VI Ly$\alpha$, O VII H$\gamma$, O VII RRC, Fe XVII 3*d*–2*p*, and Ne IX He$\delta$). We note that the flux measurements in the ACIS/Chandra spectrum are compatible with those of the EPIC/*XMM-Newton* including cases where only upper limits can be estimated in one of the spectra. In contrast with the EPIC/*XMM-Newton* spectrum, the Ne IX He$\delta$ line at 1.16 keV was not needed; instead, two more lines were added (Ne IX He$\gamma$ and Ne X Ly$\gamma$ at 1.13 and 1.22 keV, respectively) in order to get the best fit ($\chi^2 = 1.1$). Note that in the case of Ne X Ly$\gamma$ there are several transitions of Fe XX that could be contributing to this line. The inclusion of these two lines (i.e., Ne IX He$\gamma$ and Ne X Ly$\gamma$) instead of the Ne IX He$\delta$ line also provides an acceptable fit to the EPIC/*XMM-Newton* spectrum. The line intensities are reported in Table 3 (within brackets). The final fit is equally acceptable. A similar case is affecting the O VIII RRC and the Fe XVII 3*d*–2*p* lines (see Section 4.2).

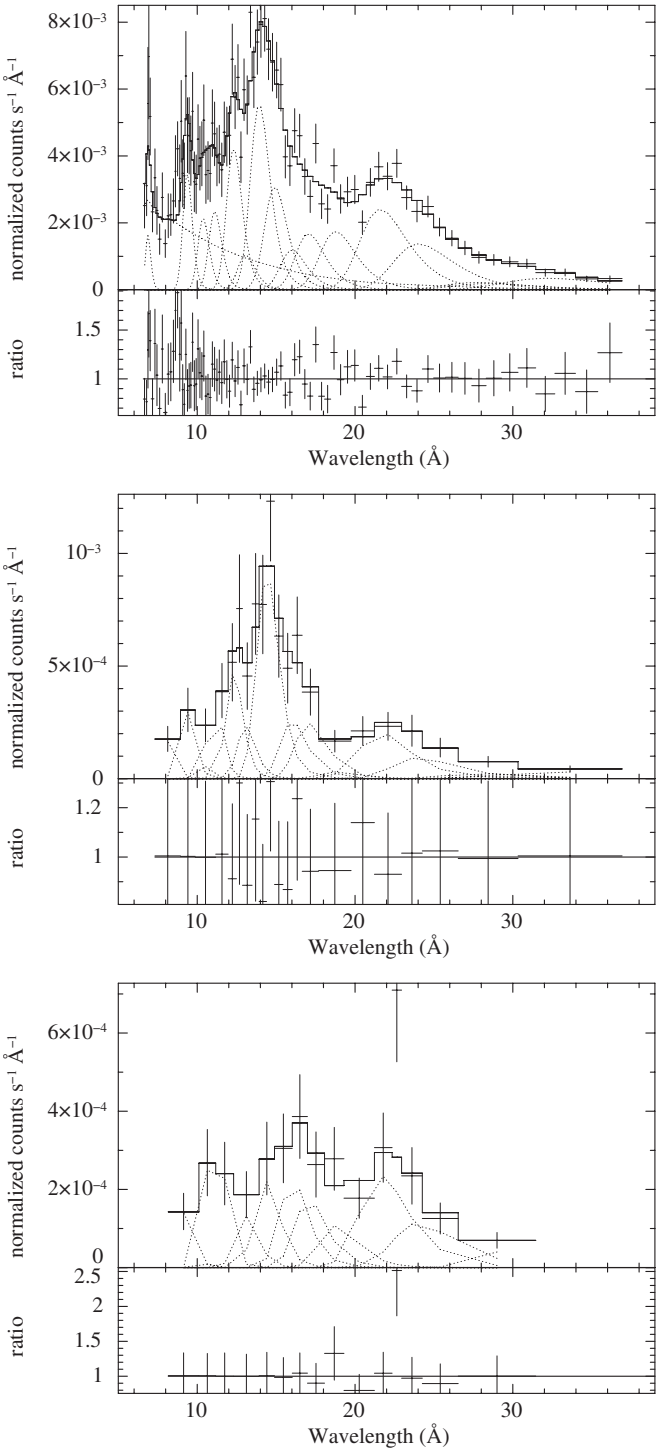


**Figure 7.** Spectral fits (top panels) and residuals (bottom panels) using low-resolution ACIS/*Chandra* spectra of the three regions: nucleus (top), cone northwest (middle), and cone southeast (bottom).

The emission lines in the northwest and southeast cones are about a factor of 10 or more, fainter than those in the nuclear region using *Chandra* data. In the northwest cone we have found the O VII triplet, O VIII RRC, Fe XX 3*d*2*p*, Ne X Ly$\alpha$,

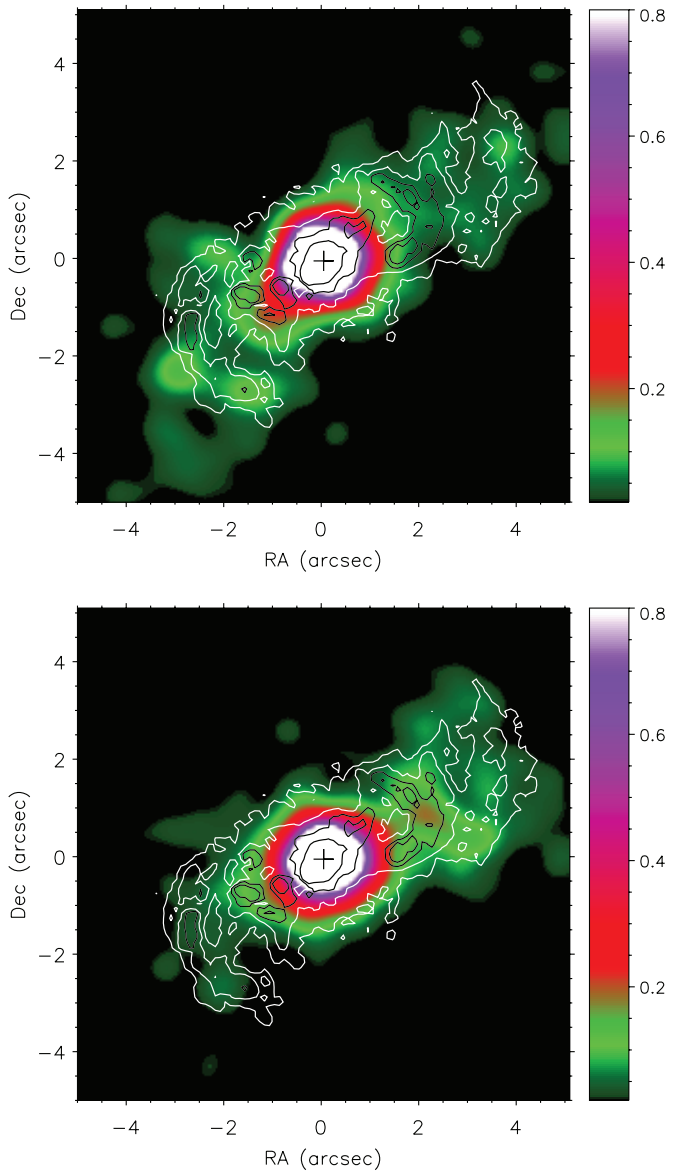


**Figure 8.** Images centered at O VII triplet (top) and O VIII RRC (bottom) lines. [O III] contours are overlaid.

(A color version of this figure is available in the online journal.)

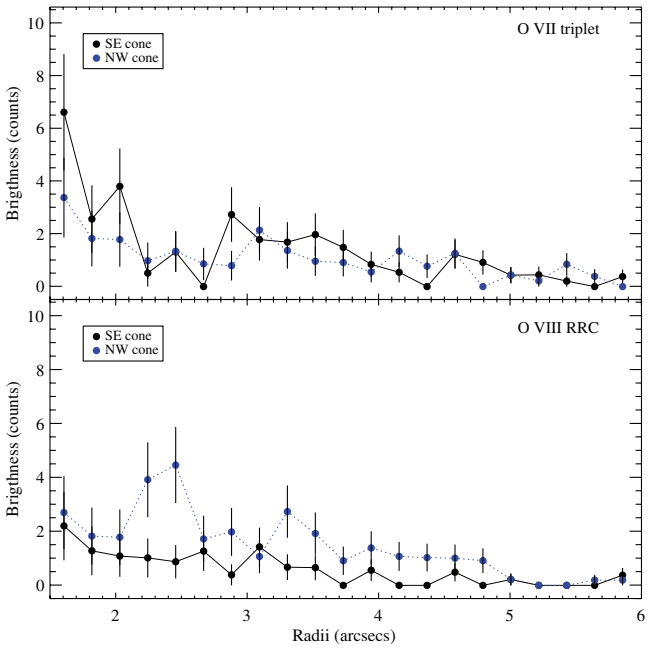


**Figure 9.** Radial profile of the images centered at the O VII triplet (top) and O VIII RRC (bottom) lines. Blue-dotted line and blue dots correspond to the northwest cone while black-continuous line and black dots correspond to the southeast cone.

(A color version of this figure is available in the online journal.)

Mg XI triplet, and Si XIII triplet. A similar result is found in the southeast cone with the detection of C V H$\gamma$, N VII Ly$\alpha$, O VII triplet, O VIII RRC, Ne IX triplet, Fe XX, Ne IX He$\delta$, and Mg XI triplet. All of these lines were detected in the ACIS/*Chandra* nuclear region, except O VIII RRC.

At first glance the spectra of the cones look rather different (see Figure 7), the northwest cone spectrum shows an enhancement around 14 Å (0.89 keV), which is not present in that of the southeast cone. To illustrate this effect we have constructed two images centered at 0.5–0.7 keV and 0.8–1.0 keV, respectively (see Figure 8). These spectral intervals are dominated by the emission of the O VII triplet at 0.569 keV and O VIII RRC at 0.871 keV, respectively (see Table 3). The O VII triplet image shows a morphology similar to that found in the soft band (<2 keV; see Figure 2). However, the O VIII RRC image shows a bright region to the northwest of the nucleus. This can also be noticed in Figure 9 where the radial profiles of the O VII triplet and O VIII RRC images are plotted. The northwest and southeast profiles appear consistent in the case of the O VII triplet, whereas there is a clear bump at 2.″5 in the northwest side of the O VIII RRC profile compared to the southeast one. Despite the limited S/N of the spectra from the cones, it seems clear that the O VIII RRC is more important in the northwest cone than in the southeast cone (see Figures 7 and 9).

## 5. ORIGIN OF THE SOFT X-RAY EMISSION

As already said, the soft X-ray spectrum of Mrk 573 is dominated by line emission, as evident from the RGS/*XMM-Newton* data (Figure 4). Emission lines from H-like and He-like C, N, O, and Ne and Fe L-shell emission-line Fe XVII dominate the spectrum, which also includes strong narrow RRC O VII and O VIII lines. The RRC features of these highly ionized species are produced when electrons recombine directly to the ground state. They are broad features for hot, collisionally ionized plasma, but are narrow, prominent features for photoionized plasma arising in low-temperature material (Liedahl & Paerels 1996; Liedahl 1999). Guainazzi & Bianchi (2007) measured in the Mrk 573 RGS spectrum the width of the RRC lines O VII and O VIII as $\sigma(\mathrm{O\,VII}) = 3.5^{+5.3}_{-3.3}$ eV and $\sigma(\mathrm{O\,VIII}) = 4.8 \pm 3.1$ eV, respectively. These values indicate a relatively cool photoionized plasma.

Relative emission strength ratios of the He-like $1s2p\,^1P_1 \rightarrow 1s^2\,^1S_0$ (r, resonance), $1s2p\,^3P_2 \rightarrow 1s^2\,^1S_0$, $1s2p\,^3P_1 \rightarrow 1s^2\,^1S_0$ (i, blended inter-combinations), and $1s2s\,^3S_1 \rightarrow 1s^2\,^1S_0$ (f, forbidden) transitions can discriminate between photoionization, collisional excitation, or hybrid environment (Porquet & Dubau 2000; Bautista & Kallman 2000; Kahn et al. 2002). A weak resonance (r) line, compared to the forbidden (f) and intercombination (i) lines, corresponds to a pure photoionized plasma. A commonly used line ratio is defined as $G = (\mathrm{f} + \mathrm{i})/\mathrm{r}$. For Mrk 573 we measured a value of $G = 1.4(0.3\text{–}12)$ for the ion O VII (see Table 2 and Figure 4). This value is lower than that expected for a pure photoionized plasma ($G > 4$), but higher than

that of collisional ionization. Such a value of $G$ would indicate a hybrid plasma where collisional processes are not negligible (Porquet & Dubau 2000), although the error bars do not allow a secure result. We could only obtain upper limits in the intensity of two of the lines needed to compute the $G$ ratio corresponding to the other ions (Ne IX and N VI) with detected He-like triplet transitions. The lower limit of $G$ obtained using Ne IX ($(f + i)/r \gtrsim 2.7$) is not conclusive although it also points to a hybrid plasma. However, the use of $G$ ratios has been questioned by several authors (e.g., Kinkhabwala et al. 2002; Porter & Ferland 2007). An important contribution of photoexcitation would raise the intensity of the resonance transition, which yields a decrease of the $G$ ratio relative to the pure photoionization case. Kinkhabwala et al. (2002) proposed the use of the ratio of higher order transitions to the forbidden triplet component in He-like ions as a good discriminant between photoexcitation and collisional ionization. Kinkhabwala et al. (2002) predicted a value of $F(\text{O VII He}\gamma)/F(\text{O VII (He}\alpha(\text{f}))$ of 0.017 for collisional ionization. Thus, an excess of He$\gamma$ line relative to the forbidden transition, as measured in Mrk 573, $F(\text{O VII He}\gamma)/F(\text{O VII (He}\alpha(\text{f}))$ = 0.31 (0.03–1.4) (see Table 2), indicates the importance of photoexcitation.

The intensities of the emission lines Fe XVII $L$ (3$d$–2$p$) and Fe XVII $K$ (3$s$–2$p$) are comparable in the case of Mrk 573 (see Table 2), which could be explained as an intermediate temperature plasma (10 eV $< kT <$ 500 eV), or under hybrid conditions combining collisional and photoionization equilibrium conditions (Liedahl et al. 1990). Similarly, Sako et al. (2000) argued that the dominance of Fe XVII L lines can only be explained if photoexcitation by the nuclear radiation plays an important role, consistent with our suggestion throughout the $G$ ratio.

From above, we conclude that the emission-line diagnostics seems to indicate that the soft-X ray spectrum of Mrk 573 as seen by RGS/*XMM-Newton* data can be produced by a plasma dominated by photoionization and photoexcitation. Nevertheless, we cannot rule out some contribution of collisional excitation, based primarily on the presence of the Fe XVII 3$d$–2$p$ transition. Unfortunately, the limited count level of the spectra does not permit us to give secure diagnostics. Detailed optical spectroscopic studies by Ferruit et al. (1999) found that ionizing photons originating in the central source are not sufficient to explain the emission-line luminosity. They suggest that fast shocks, associated with the jet/gas interactions, might contribute to the gas ionization.

The ACIS/*Chandra* spectrum of the nuclear region (1 arcsec) can be reproduced using the template obtained from the RGS/*XMM-Newton* analysis. The resulting fluxes are consistent with each other. Therefore, it seems that most of the emission-line fluxes measured in the RGS spectra come from the inner central 2 arcsec region and is consistent with the photoionization- and photoexcitation-dominated plasma scenario.

Northwest cone emission differs from that of the southwest cone and the nucleus. The O VIII RRC/O VII triplet ratio found in the northwest cone ($F(\text{OVIII RRC})/F(\text{O VII(r, i, f)}) = 0.6^{1.1}_{0.1}$) is nominally higher than in the southeast cone ($0.13^{0.56}_{0.02}$) and in the nucleus ($< 0.19$), although consistent within the statistical uncertainties. According to Kinkhabwala et al. (2002), radiative decay following photoexcitation dominates the Seyfert 2 spectrum at low column densities, whereas recombination following photoionization dominates at high column densities. Following their prescription, the RRC intensity will increase compared to He-like triplet line when column density increases, which would imply a value of $N_H$ larger for northwest than for southeast. Alternatively, the RRC line could be produced by hot collisionally ionized plasma, although the line widths reported by Guainazzi & Bianchi (2007) do not support this scenario. It is very unlikely that a broad feature contributes only in a few percentage of the total flux of source. Moreover, the radio maps of Mrk 573 are not sensitive enough to show great detail concerning radio emission, although two faint blobs are observed in the northwest cone (Falcke et al. 1998). The low S/Ns of the spectra from the cones prevent us from a more detailed study of the line transitions in the extended emission.

### 5.1. Comparison with Photoionization Models

Using version c08.00 of the Cloudy package (last described by Ferland et al. 1998), we attempted to reproduce the observed spectra of the nuclear region and northeast and southwest cones seen in ACIS/*Chandra* data.

In these Cloudy simulations, we assumed the source of ionization to emit as a typical AGN continuum (we used the model AGN available in Cloudy) defined by a "big bump" of temperature $T = 10^6$ K, an X-ray to UV ratio $\alpha_{\text{OX}} = -1.15$, plus an X-ray power law of spectral index of $\alpha = -1.0$. A plane-parallel geometry is assumed, with the slab depth controlled by the hydrogen column density parameter ($N_H$).

Two grids of parameters were constructed to simulate the expected broad-line region (BLR) and narrow-line region (NLR) conditions. For each of them, a grid of models was simulated by varying the ionization parameter ($U$), the density of the material ($N_H$), and the hydrogen column density ($N_H$). $U$ ranges from $10^{-3}$ to $10^3$, $N_H$ ranges from $10^{20}$ cm$^{-2}$ to $10^{24}$ cm$^{-2}$, and $N_H$ from $10^9$ cm$^{-3}$ to $10^{11}$ cm$^{-3}$ for BLR conditions, and from $10^2$ cm$^{-3}$ to $10^4$ cm$^{-3}$ for NLR conditions.

In both BLR or NLR models, the outputs of each Cloudy simulation include a transmitted and a reflected emission-line spectra. Under the Cloudy terminology "reflected" spectrum refers to the emission escaping into the $2\pi$ sr subtended by the illuminated face toward the ionizing source and by "transmitted" the emission escaping in the opposite direction. Each transmitted or reflected simulated emission-line spectrum is imported as additive tables ("atable") in XSPEC following Porter et al. (2006) procedure. All components are also absorbed through the Galactic value by using "wabs" on XSPEC. In practice, any additive table is included in XSPEC as follows: wabs[$N_H$(Gal)](atable{Cloudytable}), where "Cloudytable" can be transmitted/reflected for BLR/NLR conditions.

For the nuclear region, neither BLR nor NLR models produced any acceptable fit ($\chi^2_{\text{r}} = 1.9$ and $\chi^2_{\text{r}} = 1.8$, respectively). Qualitatively, the issue is that BLR and NLR models alone failed in reproducing the relative strength between 0.55 keV (the O VII triplet) and 0.9 keV (the O VIII RRC and/or Ne IX triplet). We have found that the result of our Cloudy simulations does not change with the value of the volume density and column density in the range considered here. The models are mostly sensitive to the value of the ionization parameter. Besides the two simulations for BLR and NLR conditions (hereafter called BLR and NLR models), we have also tried to model the spectrum of the nucleus as a combination of both BLR and NLR conditions (hereafter BLR+NLR model). In the BLR+NLR model, we use them all together, being then two transmitted and two reflected emission-line spectra. The combination of the BLR+NLR models produced a good fit (see Figure 10), with $\chi^2_{\text{r}} = 1.3$. The parameters of the best fit are given in Table 4. The modeled nuclear spectrum is equally dominated by the BLR and NLR emission (BLR is ~54% of the emission). We emphasize that in

**Table 4**
Best-fit Parameters to a Cloudy BLR+NLR Model

| Model Parameter | Nucleus | | Cones (Northwest/Southeast) | |
|---|---|---|---|---|
| | BLR | NLR | NLR 1 | NLR 2 |
| log ($U$) | $1.23^{1.27}_{1.18}$ | $0.13^{0.16}_{0.11}$ | $0.9 \pm 0.3/0.3 \pm 0.2$ | $-3^*/-3^*$ |
| log($n_H$) | $9.8^{10.0}_{9.7}$ | $3.14^{3.18}_{3.10}$ | $3^*$ | $3^*$ |
| log($N_H$) (cm$^2$) | $20.6^{20.7}_{20.5}$ | $20.6^{20.7}_{20.5}$ | $20^*$ | $20^*$ |
| Flux(0.5–2.0 keV) (trans.) | $35.8 \pm 9.6$ | 0.0 (<6.6) | 0.0 (<5.3) / 9.3 (<11.6) | 3.4 (<10.9) / 3.1 (<9.3) |
| Flux(0.5–2.0 keV) (reflec.) | $61.1 \pm 9.9$ | $92.6 \pm 3.7$ | 14.0 (4.6 − 23.0) / 0.0 (<14.5) | 3.8 (<10.9) / 3.0 (<9.3) |

**Notes.** Nucleus and cones. NLR1 and NLR2 refer to high- and low-ionization phases for the cones using ACIS/*Chandra* data. Fluxes in units of $10^{-15}$ erg cm$^{-2}$ s$^{-1}$.

our simulation the use of a BLR component does not necessarily imply high density material; rather, it accounts for ionization conditions higher than those of the NLR component.

In principle, we could also expect some contribution from collisionally ionized plasma (see Section 5). However, we know that this contribution should be small as indicated by the $G$ ratios, and discussed in the previous section. As an additional check, we used then this best-fit solution in order to reproduce the RGS/*XMM-Newton* spectra. We froze all the parameters adding a constant to the fit since we were mainly interested in checking whether this model could reproduce the high-resolution RGS spectra. We preferred this approach of first fitting the low-resolution spectrum and taking this as a starting point to model the high-resolution spectra. The final fit is given in Figure 11 (top) with a constant value of $1.2 \pm 0.2$. It gives a good representation of the data although it fails in reproducing the Fe XVII emission lines. Actually, the inclusion of a thermal model (APEC) with a $kT = 0.4 \pm 0.2$ keV better reproduces these features ($\Delta C \sim 14$; see Figure 11, bottom panel). In the later case, it becomes very complex to discriminate between fits due to the low count level present in the high-resolution spectrum. Based on this result, we went back to the low-resolution data and tried to fit the *Chandra* nuclear region adding the APEC component. Although it does not formally give a better fit, we obtained a fraction of the thermal component of ∼6% of the total nuclear flux. This result confirms that the thermally ionized component is present, although its contribution is small.

We have also modeled the extended emission using the grid of Cloudy simulations. In this case, we have to include the contamination from the PSF wings of the nuclear source. For this, we have computed the expected fraction of the nuclear flux contributing to the cone-like regions as $F_{\rm nuc2cone} = {\rm Flux_{PSF}(cone)/Flux_{PSF}}$ (nucleus). Assuming a Gaussian profile for the *Chandra* PSF with an FWHM of 1.2 arcsec (see Figure 1), the fraction of nuclear spectrum contributing to the cone is $F_{\rm nuc2cone} = 0.006$. This factor is equivalent to an integrated flux of $F(0.5\text{–}2.0\ {\rm keV}) = 5.06 \times 10^{-16}$ erg cm$^{-2}$ s$^{-1}$, which corresponds to 2.5% and 3.5% of the northwest and southeast cone fluxes, respectively. In order to account for this nuclear contribution we have used the BLR+NLR best-fit model found for the nucleus with all the parameters frozen, and scaled by the factor $F_{\rm nuc2cone}$. Initially we have tried to fit the cone emission by a single phase medium, using Cloudy models with NLR conditions and both reflection and transmission components. Both northwest and southeast cones have been fitted simultaneously, although the normalizations of the reflection and transmission components for the two cones are let to vary independently. The hydrogen column density and density of the material have been frozen at log ($N_H$) = 20 and log ($n_{sH}$) = 3 for simplicity. We

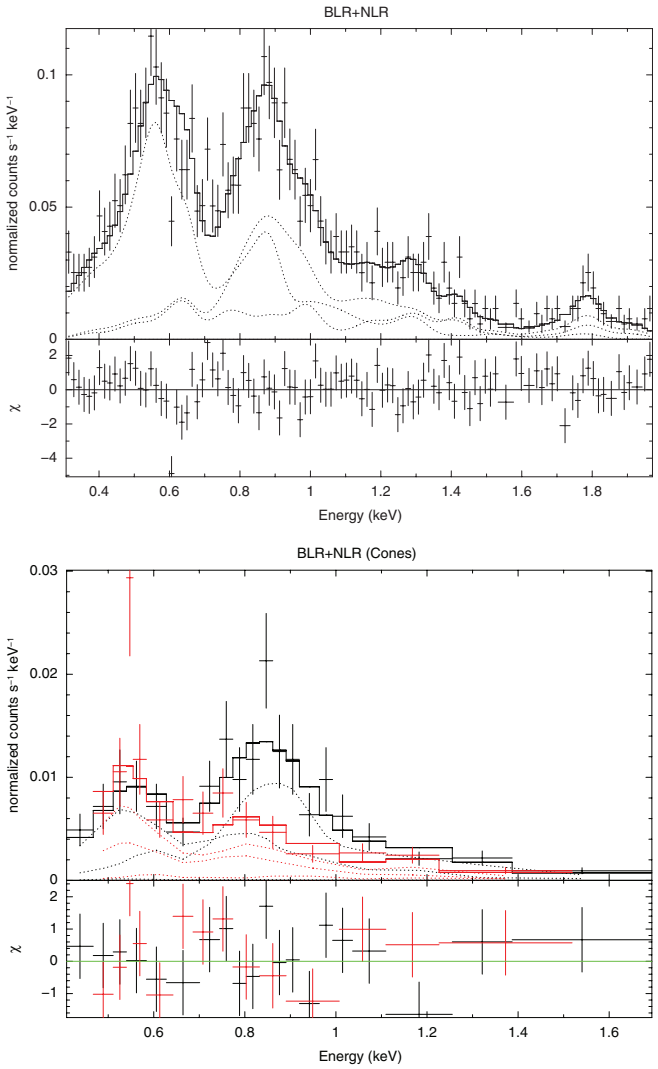


**Figure 10.** Top: ACIS/*Chandra* spectral fit and residuals to the BLR+NLR Cloudy model of the nuclear region. Bottom: same for the cone-like regions. Red (black) crosses and red (black) continuous line are the northwest (southeast) cone spectrum and fit, respectively.

(A color version of this figure is available in the online journal.)

recall that the simulated spectra by our Cloudy models are not sensitive to the value of these parameters within the explored range. The best fit shows ionization parameters of log ($U$) = $0.71 \pm 0.07$ and log ($U$) = $0.13 \pm 0.09$ for the northwest and southeast cones, respectively. Nevertheless, this fit failed to simultaneously reproduce the two spectra, since the statistics was

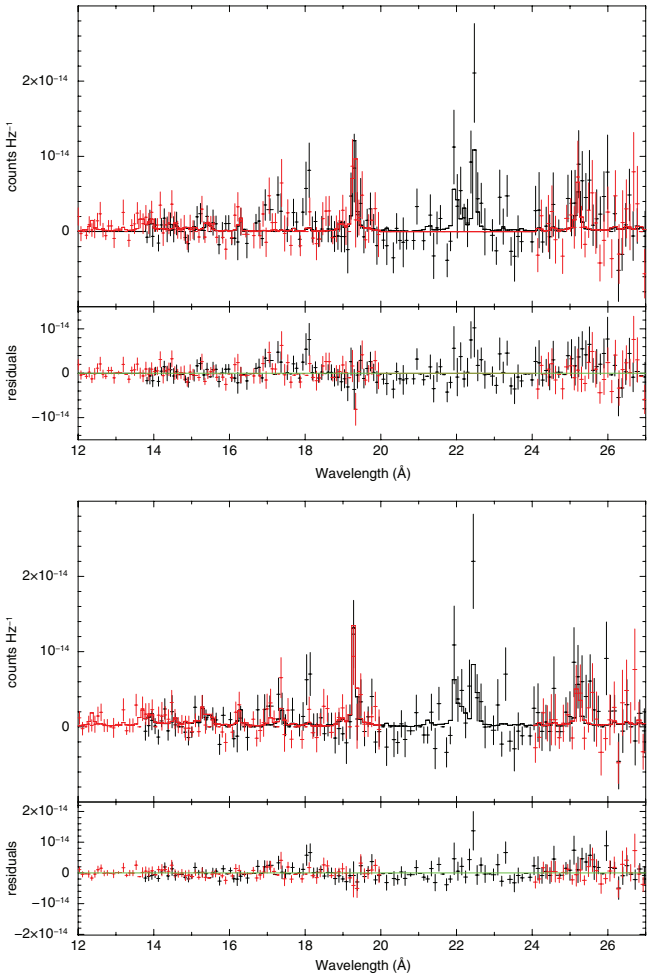


**Figure 11.** Top: RGS/*XMM-Newton* spectra fitted to the best fit found for ACIS/*Chandra* spectrum of the nuclear region (see Figure 10). Bottom: same as the top figure but with the inclusion of the thermal model APEC with $kT = 0.4 \pm 0.1$ keV.

(A color version of this figure is available in the online journal.)

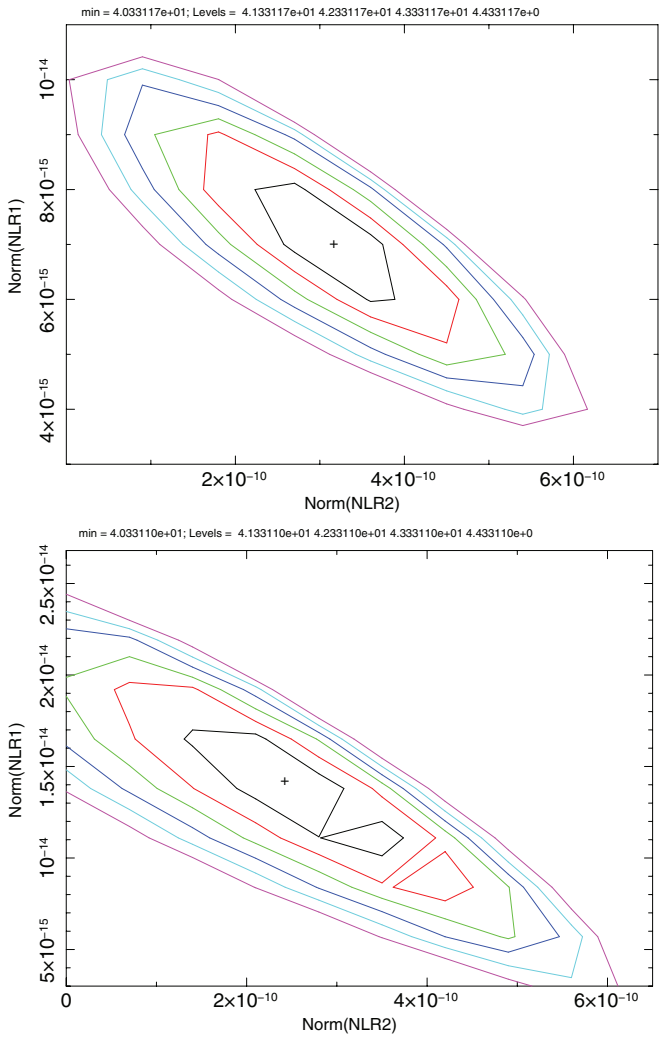


**Figure 12.** Two-dimensional iso-chi-squared flux contours of the normalization parameters of the best-fit Cloudy model of the reflected components of the northwest (top) and southeast (bottom) cones.

(A color version of this figure is available in the online journal.)

rather poor ($\chi^2_r = 1.6$). A much better fit is obtained ($\chi^2_r = 1.1$) if we add to this phase (hereafter NLR1) a second one (hereafter NLR2) with NLR conditions but with a lower value of the ionization parameter $U$. We note that due to convergence problems within XSPEC we had to freeze the ionization parameter of the second phase. We checked that the best fit is obtained for a value of log $(U) \simeq -3$ in both regions. The ionization parameters for the NLR1 phases are log $(U) = 0.9 \pm 0.2$ and log $(U) = 0.3 \pm 0.2$ for northwest and southeast cones, respectively. These values are consistent with the parameters of the previous model. The final fit can be seen in Figure 10 and the best-fit parameters and fluxes for each model component are given in Table 4. In order to show the confidence level of the fluxes, Figure 12 includes the iso-chi-squared flux contours of the normalizations of the two phases (i.e., NLR1 and NLR2) of the reflected components for the northwest (top) and southeast (bottom) cones. A similar result is obtained for the transmitted components. The NLR1 phase mostly contributes to the X-ray spectrum at the region between 0.8–0.9 keV and 0.53–0.7 keV, whereas the NLR2 phase contributes at 0.52 and 0.7–0.85 keV. The lowest value of the ionization parameter is very similar to that required to fit the optical spectrum of Mrk 573 (Kraemer et al. 2009). In that work, the authors claimed a three phase component to explain the optical emission-line spectrum. The low-ionization gas accounts for the [O II]$\lambda\lambda$3727 Å and [N II]$\lambda\lambda$6548, 6584 Å emission, whereas the moderately ionized phase accounts for the [O III]$\lambda\lambda$5007 Å. Nonetheless, our NLR1 exhibits a value of $U$ higher than their highly ionized phase. In addition, we expect a contribution of collisionally ionized plasma (see Section 5) to be present in the extended emission. However, given the fact that its contribution to the nuclear spectrum is about 6%, we assumed its contribution to the extended emission to be equal or smaller than in the nuclear case and did not try any fit given the low count level in these regions.

In terms of flux, the NLR1 phase is the 64% of the extended emission flux. Its contribution in the northwest cone is higher than in the southeast cone. Moreover, the reflection component dominates the northwest cone whereas the transmission component dominates the southeast one. Tentatively, one could attribute this result to an orientation effect, as the northwest cone is located in the farthest side while the opposite is true for the southeast one. Indeed, two-dimensional spectroscopic observations (Ferruit et al. 1999) indicates that at least part of the northwest cone's ionized gas is redshifted with respect to the systemic velocity. This could indicate that the northwest cone axis could be oriented behind the sky plane, but close to it. This

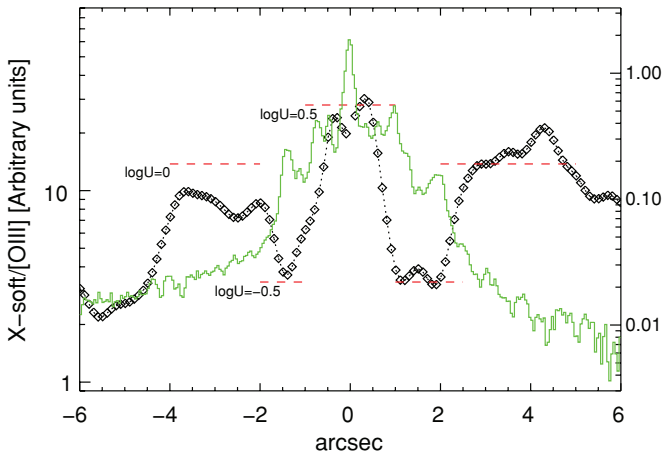


**Figure 13.** Variation of the ratio of soft X-ray to [O III] brightness profile in arbitrary units. The [O III] brightness profile variation is also overplotted as a green histogram-like line. Positive *x*-axis values indicate the northwest orientation and negative values the southeast one. Horizontal dashed lines represent predictions from simple photoionization models at various values of the ionization parameter.

(A color version of this figure is available in the online journal.)

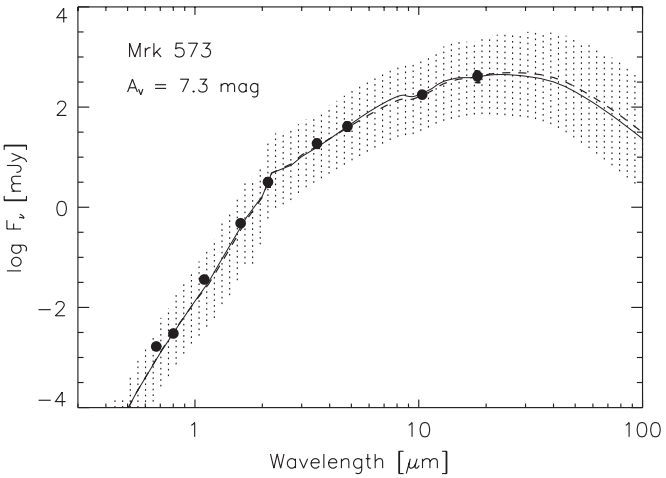


**Figure 14.** High spatial resolution nuclear SED of Mrk 573 fitted with the clumpy torus models. Solid and dashed lines are the best-fitting model and that computed with the median of each of the six parameters that describe the models (see Ramos Almeida et al. 2009a). The shaded region indicates the range of models compatible with a 68% confidence interval around the median.

orientation apparently contradicts the orientation proposed by Tsvetanov & Walsh (1992) based on reddening measurements, although we remark that their findings refer to the orientation with respect to the galaxy disk, not to the sky plane. Remarkably, the NLR2 phase accounts for the same flux in the northwest and southeast cones and nearly equal relative contribution of the reflection and transmission components. Thus, this low-ionization phase seems to be uniformly distributed along the cone area.

At this point, we may conclude that soft extended X-ray emission is then powered by features coming from ionized gas in two phases under NLR-like conditions. Furthermore, one may question: is the [O III] extended emission structure powered by the same mechanism? The similarity between the [O III] structures and the soft X-ray emission points to a common origin for both components. We have investigated the radial variation of the ratio between the soft X-ray and the [O III] line emission. We presented in Figure 13 the variation of the brightness ratio along the axis of the cone (P.A. $= 122^{\circ}$). The brightness profiles were extracted using the IRAF *pvector* task. Before obtaining the ratio we convolved the [O III] profile to obtain the resolution of X-ray data. As can be seen from Figure 13 the soft-X/[O III] ratio presents a non-uniform variation showing a maximum at the nucleus; it then drops dramatically at the position of the [O III] arcs and returns at roughly half of the nuclear value outside the [O III] arcs. A similar behavior, namely, a small variation of the ratio, has been reported by Bianchi et al. (2006) for the case of NGC 3393. We have also compared the radial variation with predictions from photoionization models in Figure 13. We have used simple models assuming single plane-parallel slabs, constant density, and radiation bounded clouds. The soft X-ray emission has been taken as the sum of the predicted values for the most intense features identified in our X-ray spectra. We have scaled the model predictions to the observed nuclear values from the model with $\log U = 0.5$, which is close to the best-fitting value derived above. The predictions for different values of the ionization parameters are represented in Figure 13. It can be seen that a variation of $U_t$ by 1 order of magnitude is needed to reproduce the observed variation in the brightness ratio from the nucleus to the arcs, which could be attributed to a combination of radiation dilution plus density enhancements at the arc positions. Note that these variations are qualitatively in agreement with our Cloudy model simulations in which two different $U$ values are needed for the southeast and northwest cones. A baseline model where the density decreases as $r^{-2}$, as proposed by Bianchi et al. (2006), is compatible with our results, except for the regions close to the [O III] arcs. It is very likely that simple photoionization models are not adequate to reproduce the observed ionization variations, although a more sophisticated treatment must wait until higher quality X-ray spectroscopic observations become available. The fact that ionization- and matter-bounded clouds are likely constituents of the NLR has not been explored to explain emission lines in the soft-X range.

## 6. THE NUCLEAR SPECTRAL ENERGY DISTRIBUTION

Another important feature of the unified model is the optically thick torus. Under this scheme, type 2 Seyferts like Mrk 573 are obscured due to this material being located along our line of sight. The best way to study and characterize the molecular torus is by modeling the nuclear SED of the sources. The near- and mid-IR nuclear emission of Seyfert galaxies is attributed to the reprocessing of the UV/X-ray nuclear radiation by the toroidal dusty structure. For this reason, the infrared range is key to putting constraints on torus modeling. However, in comparing the predictions of any torus model with observations, the small-scale torus emission must be isolated, in order to avoid contamination from the host galaxy. For this reason, it is important to use high angular resolution data when trying to model the torus emission.

We have tried here to explain the optical/infrared nuclear SED of Mrk 573 constructed with high spatial resolution data (see Table 1) using an interpolated version of the recent models for the clumpy torus scenario by Nenkova et al. (2008b, 2008a). We have searched for the best-fitting models using the Bayesian inference tool BayesClumpy (Asensio Ramos & Ramos Almeida 2009). The results of the fit are shown in Figure 14.

Indeed, the nuclear SED of Mrk 573 has been previously fitted by Ramos Almeida et al. (2009a) using this set of models and tools, although the data points below 1 $\mu$m were not included in their analysis. To use the optical photometry derived in this

work, the clumpy torus model fit needs an additional extinction factor, which is included as a foreground extinction. The derived median value is $A_V = 7.3 \pm 0.5$ mag, which can be translated to a column density of $N_H = 1.39 \times 10^{22}\,\mathrm{cm}^{-2}$. This value is nicely consistent with that derived from the optical color–color maps (see Section 3).

The results of the fitting process are the probability distributions for the free parameters that describe the clumpy models (see Ramos Almeida et al. 2009a). For Mrk 573, the median values of the parameters correspond to a torus width of 30°, $N_0 = 4 \pm 1$ clouds in the equatorial direction, optical depth per single cloud $\tau_V \sim 60$, and $A_V^{\mathrm{LOS}} \sim 300$ mag (equivalent to $N_H^{\mathrm{LOS}} \sim 5.7 \times 10^{23}\,\mathrm{cm}^{-2}$). These torus parameters are similar to those derived without including the optical data points by Ramos Almeida et al. (2009a).

We have determined the torus luminosity integrating the corresponding emission from the torus model corresponding to the median value of the probability distribution of each parameter (dashed line in Figure 14). The resulting value is $L_{\mathrm{bol}}^{\mathrm{tor}} = 7.4 \times 10^{43}\,\mathrm{erg\,s}^{-1}$. The clumpy model fit yields the bolometric luminosity of the intrinsic AGN, $L_{\mathrm{bol}}^{\mathrm{AGN}} = 5.2 \times 10^{44}\,\mathrm{erg\,s}^{-1}$ (the bolometric luminosities are good to a factor of 2). Combining this value with the torus luminosity, we derive the reprocessing efficiency of the torus, which for Mrk 573 is quite low, about 14%.

Moreover, we have derived the X-ray luminosity from the hard X-ray part, assuming a power law with photon index 1.8. The range from 2 to 6 keV was used to avoid, on the one hand the soft range, which is attributed to emission lines, and the Fe K line, on the other. The galactic absorption plus an intrinsic absorption were included in the fitting process. The intrinsic absorption results in a value of $N_H = 7^{+6}_{-5} \times 10^{22}\,\mathrm{cm}^{-2}$, which is compatible with the foreground extinction inferred from the color maps and the clumpy torus modeling. Thus, the absorption corrected X-ray luminosity is $L_{2-10\,\mathrm{keV}} = 1.7 \times 10^{41}\,\mathrm{erg\,s}^{-1}$. This value is quite low when compared to the optical/infrared luminosity reprocessed by the blocking torus. However, it can be reconciled by taking into account that Mrk 573 has been classified as a Compton-thick AGN (Guainazzi et al. 2005), and its X-ray luminosity has to be corrected by a large factor to obtain the intrinsic luminosity, since the column density is $N_H > 1.6 \times 10^{24}\,\mathrm{cm}^{-2}$ (such high value of the optical depth is also consistent with the value derived above from the clumpy torus modeling). Panessa et al. (2006) derived a factor of 60 comparing a small sample of Compton-thick type 2 Seyferts with a sample of type 1 Seyferts, whereas Cappi et al. (2006) derived a factor of about 100. These values are in contrast with the work of González-Martín et al. (2009), who obtained a value of 42 using a sample of LINERs. In addition, we have to transform from X-ray to bolometric luminosity multiplying by a factor of 30 (Risaliti & Elvis 2004; see also Panessa et al. 2006). Thus, we obtain a value for the bolometric AGN luminosity in the range $L_{\mathrm{AGN}}^{\mathrm{bol}} = (3.1\text{–}5.1) \times 10^{44}\,\mathrm{erg\,s}^{-1}$, which is in nice agreement with the value derived from the torus reprocessing, given the uncertainties involved. Kraemer et al. (2009) derived a higher value for the bolometric luminosity ($3.2 \times 10^{45}\,\mathrm{erg\,s}^{-1}$) based on the [O IV] 25.9 $\mu$m luminosity, as measured by the *Spitzer*/IRS spectrum of Mrk 573 (Meléndez et al. 2008a, 2008b). In any case, Mrk 573 seems to be radiating near the Eddington limit, assuming the black hole mass is around $2 \times 10^7\,M_\odot$ (Bian & Gu 2007). This result adds support to the re-classification of Mrk 573 as a hidden narrow-line Seyfert 1 (Ramos Almeida et al. 2008).

## 7. CONCLUSIONS AND OVERALL PICTURE

Mrk 573 is a nearby optically classified type 2 Seyfert, well known for its extended circumnuclear emission-line regions. It is this extension and the proximity of the source that convert Mrk 573 as one of the ideal cases to study this emission commonly found in type 2 Seyfert galaxies. We combine RGS/*XMM-Newton* and ACIS/*Chandra* to achieve high spectral and spatial resolution in order to disentangle the emission mechanism of this extended emission. We also used optical and near-IR *HST* data in order to compare with the X-ray data. The main results are as follows.

1. The soft X-ray emission is very complex, resembling that of the [O III] emission, as already reported. What constitutes our new result is that the northwest structure specifically is also very similar to that of the [O III]/H$\alpha$ emission. This suggests the same origin for the emission lines at the optical and soft X-ray ranges.
2. Through X-ray spectroscopic analysis we have found that plasma excitation mechanism in the nuclear spectrum is mainly driven by photoionization from the central source, including a strong contribution from photoexcitation. A small contribution of collisionally ionized plasma is also needed to explain the emission-line ratios shown by RGS spectra. This conclusion also agrees with the proposed Cloudy simulations since the spectra could be interpreted as the combination of two different phases of Cloudy models, with two different ionization parameters $\log(U) = 1.23$ and $\log(U) = 0.13$.
3. Based on the ACIS/*Chandra* images and radial profiles along the O VII triplet and O VIII RRC for cone-like structures, we showed that the O VIII RRC could be more relevant toward the northwest cone, although the line ratios are formally compatible after including the error bars.
4. We have successfully modeled the cone-like emission using Cloudy simulations corresponding to two phases of NLR conditions. The first phase shows different values of ionization parameter and different contributions of the reflected and transmitted components for the northwest ($\log(U) = 0.9$; reflected dominated) and southeast ($\log(U) = 0.3$; transmitted dominated) cones. The second is a homogeneous phase with a lower ionization parameter ($\log(U) = -3$) and the same contribution of reflected and transmitted components for the northwest and southeast cones.
5. We have found a good agreement between the AGN bolometric luminosity derived from the hard X-ray luminosity and the one derived from the modeling of the optical/infrared SED with a clumpy torus model.
6. From the extinction maps we have found that a dust lane crosses the nucleus in the north–south direction. This could be, in projection, perpendicular to the direction of the cone-like structure. The amount of extinction we have derived from this map is also consistent with that derived from the SED modeling. However, this must be related with the extended extinction since, in the inner parts, the AGN is hidden by a column density on the Compton-thick regime ($N_H > 1.6 \times 10^{24}\,\mathrm{cm}^{-2}$).

We thank the anonymous referee for helpful comments that have improved the final manuscript. Financial support through the grants AYA2006-09959, AYA2007-60235, and AYA2008-06311-C02-01 from Plan Nacional de Astronomía y Astrofísica

is acknowledged. O.G.M. acknowledges support by the EU FP7-REGPOT 206469 and ToK 39965 grants. C.R.A. acknowledges financial support from STFC PRDA (ST/G001758/1). The authors acknowledge the Spanish Ministry of Science and Innovation (MICINN) through the Consolider-Ingenio 2010 Program grant CSD2006-00070: First Science with the GTC (http://www.iac.es/consolider-ingenio-gtc/). O.G.M. acknowledges A. Nucita's help in using Cloudy models. The authors acknowledge Andrés Asensio Ramos for his valuable help and cooperation related with the use of BayesClumpy. Based on observations made with the NASA/ESA *Hubble Space Telescope*, and obtained from the Hubble Legacy Archive, which is a collaboration between the Space Telescope Science Institute (STScI/NASA), the Space Telescope European Coordinating Facility (ST-ECF/ESA) and the Canadian Astronomy Data center (CADC/NRC/CSA).

*Note added in manuscript.* After this paper was submitted to the journal, a paper was published by Bianchi et al. (2010) with data in common with our work. Most of their results are consistent with ours, although different approaches were used. They fitted the *XMM-Newton*/RGS spectra using Cloudy photoionization models. Their best fit was obtained by a hybrid model—photoionization + collisional excitation—where the collisional phase contributes 1/3 of the flux in the 0.5–0.8 keV band, consistent with our work. Moreover, they claimed a need for two photoionization phases ($\log U = 0.3$ and 1.8) to explain the ACIS/*Chandra* spectrum in the range 0.4–7 keV, which is also in agreement with our results. The results on the extended emission cannot be compared since they do not distinguish between the two cone-like structures, extracting the spectrum from a circumnuclear annulus.

## REFERENCES

Alonso-Herrero, A., Quillen, A. C., Rieke, G. H., Ivanov, V. D., & Efsthatiou, A. 2003, AJ, 126, 81
Antonucci, R. R. J. 1993, ARA&A, 31, 473
Arnaud, K. A. 1996, in ASP Conf. Ser. 101, Astronomical Data Analysis Software and Systems V, ed. G. H. Jacoby & J. Barnes (San Francisco, CA: ASP), 17
Asensio Ramos, A., & Ramos Almeida, C. 2009, ApJ, 696, 2075
Bautista, M. A., & Kallman, T. R. 2000, ApJ, 544, 581
Bian, W., & Gu, Q. 2007, ApJ, 657, 159
Bianchi, S., Chiaberge, M., Evans, D. A., Guainazzi, M., Baldi, R. D., Matt, G., & Piconcelli, E. 2010, MNRAS, 405, 553
Bianchi, S., Guainazzi, M., & Chiaberge, M. 2006, A&A, 448, 499
Bock, J. J., et al. 2000, AJ, 120, 2904
Burrows, D. N., et al. 2000, ApJ, 543, L149
Cappi, M., et al. 2006, A&A, 446, 459
Crenshaw, D. M., Kraemer, S. B., Boggess, A., Maran, S. P., Mushotzky, R. F., & Wu, C.-C. 1999, ApJ, 516, 750
Crenshaw, D. M., Kraemer, S. B., & George, I. M. 2003, ARA&A, 41, 117
Dai, X., Mathur, S., Chartas, G., Nair, S., & Garmire, G. P. 2008, AJ, 135, 333
Ebeling, H., White, D. A., & Rangarajan, F. V. N. 2006, MNRAS, 368, 65
Evans, D. A., Lee, J. C., Kamenetska, M., Gallagher, S. C., Kraft, R. P., Hardcastle, M. J., & Weaver, K. A. 2006, ApJ, 653, 1121
Falcke, H., Wilson, A. S., & Simpson, C. 1998, ApJ, 502, 199
Ferland, G. J., Korista, K. T., Verner, D. A., Ferguson, J. W., Kingdon, J. B., & Verner, E. M. 1998, PASP, 110, 761
Ferruit, P., Wilson, A. S., Falcke, H., Simpson, C., Pécontal, E., & Durret, F. 1999, MNRAS, 309, 1
Gabriel, C., et al. 2004, in ASP Conf. Ser. 314, Astronomical Data Analysis Software and Systems (ADASS) XIII, ed. F. Ochsenbein, M. G. Allen, & D. Egret (San Francisco, CA: ASP), 759
González-Martín, O., Masegosa, J., Márquez, I., & Guainazzi, M. 2009, ApJ, 704, 1570
Guainazzi, M., & Bianchi, S. 2007, MNRAS, 374, 1290
Guainazzi, M., Bianchi, S., Cappi, M., Dadina, M., & Malaguti, G. 2008, RevMexAA Conf. Ser., 32, 96
Guainazzi, M., Matt, G., & Perola, G. C. 2005, A&A, 444, 119
Hopkins, P. F., Robertson, B., Krause, E., Hernquist, L., & Cox, T. J. 2006, ApJ, 652, 107
Kahn, S. M., Behar, E., Kinkhabwala, A., & Savin, D. W. 2002, Proc. R. Soc. A, 360, 1923
Kauffmann, G., et al. 2003, MNRAS, 346, 1055
Kinkhabwala, A., et al. 2002, ApJ, 575, 732
Kinney, A. L., Schmitt, H. R., Clarke, C. J., Pringle, J. E., Ulvestad, J. S., & Antonucci, R. R. J. 2000, ApJ, 537, 152
Kraemer, S. B., Schmitt, H. R., & Crenshaw, D. M. 2008, ApJ, 679, 1128
Kraemer, S. B., Trippe, M. L., Crenshaw, D. M., Meléndez, M., Schmitt, H. R., & Fischer, T. C. 2009, ApJ, 698, 106
Krist, J. 1993, in ASP Conf. Ser. 52, Astronomical Data Analysis Software and Systems II, ed. R. J. Hanisch, R. J. V. Brissenden, & J. Barnes (San Francisco, CA: ASP), 536
Liedahl, D. A. 1999, in X-Ray Spectroscopy in Astrophysics, ed. J. van Paradijs & J. A. M. Bleeker (Berlin: Springer), 189
Liedahl, D. A., Kahn, S. M., Osterheld, A. L., & Goldstein, W. H. 1990, ApJ, 350, L37
Liedahl, D. A., & Paerels, F. 1996, ApJ, 468, L33
Meléndez, M., Kraemer, S. B., Schmitt, H. R., Crenshaw, D. M., Deo, R. P., Mushotzky, R. F., & Bruhweiler, F. C. 2008a, ApJ, 689, 95
Meléndez, M., et al. 2008b, ApJ, 682, 94
Moriondo, G., Giovanelli, R., & Haynes, M. P. 1998, A&A, 338, 795
Nenkova, M., Sirocky, M. M., Ivezić, Ž., & Elitzur, M. 2008a, ApJ, 685, 147
Nenkova, M., Sirocky, M. M., Nikutta, R., Ivezić, Ž., & Elitzur, M. 2008b, ApJ, 685, 160
Ogle, P. M., Brookings, T., Canizares, C. R., Lee, J. C., & Marshall, H. L. 2003, A&A, 402, 849
Ogle, P. M., Marshall, H. L., Lee, J. C., & Canizares, C. R. 2000, ApJ, 545, L81
Panessa, F., Bassani, L., Cappi, M., Dadina, M., Barcons, X., Carrera, F. J., Ho, L. C., & Iwasawa, K. 2006, A&A, 455, 173
Peng, C. Y., Ho, L. C., Impey, C. D., & Rix, H.-W. 2002, AJ, 124, 266
Plucinsky, P. P., et al. 2008, Proc. SPIE, 7011, 70112E
Pogge, R. W., & De Robertis, M. M. 1993, ApJ, 404, 563
Porquet, D., & Dubau, J. 2000, A&AS, 143, 495
Porter, R. L., & Ferland, G. J. 2007, ApJ, 664, 586
Porter, R. L., Ferland, G. J., Kraemer, S. B., Armentrout, B. K., Arnaud, K. A., & Turner, T. J. 2006, PASP, 118, 920
Quillen, A. C., Alonso-Herrero, A., Rieke, M. J., McDonald, C., Falcke, H., & Rieke, G. H. 1999, ApJ, 525, 685
Ramos Almeida, C., Levenson, N. A., Alonso-Herrero, A., Asensio Ramos, A., Radomski, J. T., Packham, C., Fisher, R. S., & Telesco, C. M. 2009a, ApJ, 702, 1127
Ramos Almeida, C., Pérez García, A. M., & Acosta-Pulido, J. A. 2009b, ApJ, 694, 1379
Ramos Almeida, C., Pérez García, A. M., Acosta-Pulido, J. A., & González-Martín, O. 2008, ApJ, 680, L17
Ramos Almeida, C., Pérez García, A. M., Acosta-Pulido, J. A., Rodríguez Espinosa, J. M., Barrena, R., & Manchado, A. 2006, ApJ, 645, 148
Risaliti, G., & Elvis, M. 2004, in Supermassive Black Holes in the Distant Universe, ed. A. J. Barger (Dordrecht: Kluwer), 308, 187
Ruiz, J. R., et al. 2005, AJ, 129, 73
Sako, M., Kahn, S. M., Paerels, F., & Liedahl, D. A. 2000, ApJ, 543, L115
Schawinski, K., Virani, S., Simmons, B., Urry, C. M., Treister, E., Kaviraj, S., & Kushkuley, B. 2009, ApJ, 692, L19
Schawinski, K., et al. 2007, MNRAS, 382, 1415
Schlesinger, K., Pogge, R. W., Martini, P., Shields, J. C., & Fields, D. 2009, ApJ, 699, 857
Schmitt, H. R., Donley, J. L., Antonucci, R. R. J., Hutchings, J. B., & Kinney, A. L. 2003, ApJS, 148, 327
Silk, J., & Rees, M. J. 1998, A&A, 331, L1
Strüder, L., et al. 2001, A&A, 365, L18
Tsvetanov, Z., & Walsh, J. R. 1992, ApJ, 386, 485
van Dokkum, P. G. 2001, PASP, 113, 1420
Veilleux, S., Shopbell, P. L., Rupke, D. S., Bland-Hawthorn, J., & Cecil, G. 2003, AJ, 126, 2185
Whittle, M., & Wilson, A. S. 2004, AJ, 127, 606
Yang, Y., Wilson, A. S., & Ferruit, P. 2001, ApJ, 563, 124
Young, A. J., Wilson, A. S., & Shopbell, P. L. 2001, ApJ, 556, 6